Rationale of GNSS Reflected Delay–Doppler Map (DDM) Distortions Induced by Specular Point Inaccuracies

Giuseppe Grieco 🔗, Ad Stoffelen 🔗, *Senior Member, IEEE*, and Marcos Portabella 🔗

Abstract—Global navigation satellite system reflectometry (GNSS-R)-derived winds from the cyclone GNSS (CYGNSS) satellite constellation are expected to significantly improve weather forecasts in the tropical region. Delay–Doppler maps (DDMs) acquired by the TechDemosat-1 (TDS-1) GNSS-R satellite mission suffer from distortions that are highly correlated to on-board specular point estimation inaccuracies. Such distortions may affect wind retrievals, especially when multilook approaches aiming at exploiting the ambiguity-free area of the DDM are applied. This article demonstrates: that CYGNSS DDMs are also affected by such distortions; the rationale of DDM shape asymmetries induced by specular point location inaccuracies; and a simple strategy for reducing such induced distortions. Two different datasets have been used, consisting of both regular and raw intermediate frequency CYGNSS measurements. The results show that, similar to TDS-1, the CYGNSS DDM distortions are correlated to specular point location inaccuracies. Furthermore, such inaccuracies are significantly reduced if more accurate specular point related parameters are used to recompress the raw GNSS-R echo, highlighting some sampling issues that are common to both TDS-1 and CYGNSS missions. These results suggest that multilook wind retrieval approaches aiming at exploiting also the peripheral parts of the DDM may be seriously compromised by such distortions. The latter may be substantially reduced by oversampling the outcoming DDM and by *a posteriori* choosing the proper DDM subsample. For future upcoming GNSS-R missions, it is strongly recommended to store the raw data for eventual reprocessing in case of miscalibration or processing issues such as those shown in this article.

Index Terms—Delay–Doppler map (DDM) distortions, global navigation satellite system (GNSS), reflectometry.

I. INTRODUCTION

GLOBAL navigation satellite system reflectometry (GNSS-R)-derived winds are expected to give a remarkable contribution to weather forecasts both in extreme and nominal wind conditions. GNSS-R potentially represents an attractive complementary wind source to other more consolidated, such as scatterometers [1], for several reasons: first, the low cost of missions; second, the potentially high availability of measurements of opportunity due to the highly populated GNSS constellations; and third, the very low sensitivity of *L*-band measurements to precipitations. The accuracy of weather forecasts depends on the accuracy of the wind acquisitions to be assimilated in numerical weather prediction (NWP) models, on their coverage, and on temporal sampling [2]. GNSS-R-derived winds are not expected to overcome or even equalize scatterometer winds accuracy, but they can be profitably used to cover the time lags of the scatterometer constellation for data assimilation purposes [3]. Two GNSS-R missions have proven the capability of measuring wind speed from space: the U.K. polar orbiting satellite TechDemosat-1 (TDS-1) [4] and the U.S. constellation of eight nanosatellites cyclone GNSS (CYGNSS) [5]. While TDS-1 has been designed to prove the feasibility of GNSS-R satellite missions, CYGNSS is the first scientific satellite mission employing such technology for monitoring tropical cyclones (TCs) [5]. CYGNSS has been designed in order to have low sensitivity to rainfalls and high revisit time in the tropical belt. Both features will hopefully help to improve the forecast of both kinematics and thermodynamics of TCs.

A few studies have shown the potentiality of CYGNSS wind speed assimilation in NWP models for hurricane forecasts by using simulated CYGNSS winds [6]–[9]. All of them agree on the potentiality of CYGNSS wind speed assimilation in improving both kinematic and thermodynamic features of TC forecasts. While this article is being written, only Cui *et al.* [10] show a study based on real CYGNSS wind speed assimilation in forecast experiments. These experiments relate to hurricanes Harvey and Irma, which made landfall on U.S. coasts during summer 2017. The authors conclude that more has to be done in order to improve the accuracy of CYGNSS wind speed, looking forward newer versions of data. Park *et al.* [11] have focused on the possibility to exploit CYGNSS-derived wind speeds for detecting convective cells. The authors conclude that, thanks to the short revisit time, CYGNSS measurements can potentially be helpful for such purpose. Once more, this article stresses the need to improve the accuracy of CYGNSS wind retrievals.

The accuracy of CYGNSS-derived wind speeds is claimed to be around 1.4 ms^{-1} in the range of 0–20 ms^{-1} according to [12]. This figure comes out from a root-mean-square error (RMSE) assessment by comparing CYGNSS winds with forecast winds of the European Centre for Medium-Range Weather Forecasts (ECMWF). However, the authors also note that CYGNSS winds are biased and the latter is not constant in the aforementioned wind speed range, and it remarkably increases above 10 ms^{-1}. Moreover the RMSE is not constant either, being higher than 3 ms^{-1} for wind speeds higher than 15 ms^{-1}. Since the wind speed distribution over the ocean is similar to a Rayleigh distribution, peaking around 6–7 ms^{-1}, the highly biased wind speed range has a lower weight in the accuracy computation.

It comes out that several systematic errors are still present in the calibration procedure, which propagate in the wind speed retrievals. This is still work in progress for the engineers and scientists of the CYGNSS mission. Such features are similar to TDS-1-derived winds [13]. An extensive overview of miscalibration features of CYGNSS winds is reported in [14]. It is important to stress that the authors analyze version 2.0 of CYGNSS winds, before the $L1$ calibration scheme had been updated according to [15] and [16], which gave rise to version 2.1. The sources of miscalibration may be numerous. In [15], a discussion on the mitigation of calibration issues due to a poor collocation of the scattering area used to normalize the bistatic radar cross section (BRCS) is shown. Furthermore, a more efficient weighting procedure leading to a more accurate normalized BRCS, the so-called delay–Doppler map (DDM) average (DDMA), is described. The effects of the GPS equivalent isotropic radiative power inaccuracies are taken into account in [16]. An equivalent procedure for TDS-1 measurements is presented in [17]. Wang *et al.* [18] focus their attention on the distortions caused by a misrefreshing of the correlation window on each coherent integration step, and propose a postprocessing methodology aimed at reducing such effects. Such misalignments are caused by the high variability of both low earth orbit receivers and GNSS transmitters orbital parameters. They demonstrate their reconstruction methodology with DDMs from TDS-1, but it is likely that such effects are also present in CYGNSS DDMs. Li *et al.* [19] demonstrate how PRN-dependent deviations of the autocorrelation function (ACF) can lead to biases in the CYGNSS observables DDMA and leading edge slope (LES). Such deviations are due to the sidelobes of the ACF that are not taken into account during the DDM computation. The resulting DDMA biases may amount to 0.5 dB, which can lead to a retrieved wind speed bias of about 10%. It has been recently demonstrated that TDS-1 DDMs are affected by some shape distortions that are strictly correlated to on-board SP location estimate inaccuracies [20]. On-board estimations of the SP location come out from a fast algorithm that implements the so-called quasi-spherical (QS) approximation of the earth surface [21]. This algorithm is implemented in both TDS-1 and CYGNSS receivers, since both missions share the same space GNSS receiver remote sensing instruments (SGR-ReSI), provided by the U.K. Surrey Satellite Technology Limited (SSTL). The accuracy of such estimates is within approximately ±200 Hz for TDS-1

TABLE I
GNSS-R MISSIONS FROM THE POINT OF VIEW OF WEATHER FORECASTS

Mission	Orbit	Revisit Time	RMSE$_{[0-20ms^{-1}]}^{MAX}$ (<2 ms^{-1})	Issues
CYGNSS	$\theta \approx 35^o$	High	>3 ms^{-1}	Cal [14], corr window [18]
TDS-1	Polar	Low	> 3ms^{-1}	ACF$_{PRN}$ [19] SP [20]

2 ms^{-1} is the recommended maximum value of RMSE in the whole range between 0 and 20 ms^{-1}. The column "issues" represents the shared problems that still hamper to reach this value.

and ±150 Hz for CYGNSS, whose differences are likely to be attributable to the different orbital features. Such inaccuracies may affect the observables of both missions, but, to the best of our knowledge, such kind of study has not yet been carried out. It is important to stress that the distortions that are discussed here are not taken into account by the "repositioning" algorithm implemented by [15]. Here, the authors accurately locate the SP projection in the DDM for a more accurate computation of the scattering area. The distortions that are discussed here concern the correlation of the PRN replica with the reflected GNSS signal, which may give rise to sampling issues. Since such distortions affect the DDM shape, they may seriously compromise the multilook approaches aiming at exploiting the ambiguity-free zone of the DDM, the so-called "horse shoe," if such effects are not taken into account in a forward model of the DDM. Among these methods, it is worth to cite the so-called stare processing shown in [22].

Since both TDS-1 and CYGNSS payloads share SGR-ReSI, it is expected that CYGNSS DDMs suffer from the same distortions as TDS-1 DDMs. The demonstration of such thesis is the first aim of this article. The second aim is the demonstration of the rationale for which SP inaccuracies cause DDM shape distortions.

How much such distortions affect both operational and alternative GNSS-R observables [23]–[25] is beyond the scope of this article. A thorough study on this topic is left for the upcoming future. However, a preliminary assessment of such impacts and the impacts on altimetric applications is provided.

Table I can help to better understand the point of view of weather forecasters for what concerns the exploitation of GNSS-R-derived winds. The last column of this table remarks the most challenging issues common to both TDS-1 and CYGNSS that, in our opinion, still hamper a proper exploitation of satellite GNSS-R measurements. The rest of this article is organized as follows. Section II recalls the theoretical framework of this article. Section III describes the employed datasets and the methodology. Section IV reports on the results of the experiments. A thorough discussion about the findings and the future plans is shown in Section V and, finally, Section VI draws the conclusions.

II. BACKGROUND

It is well known that the DDM represents the distribution of the reflected GNSS incoming power among a set of delay–Doppler bins. It is obtained by first cross-correlating the reflected

field with the PRN replica code of the GNSS transmitter according to the correlation integral depicted in (1), and then by taking its squared value [26]:

$$
\begin{aligned}
Y(\tau, \Delta f) \\
&= \int_0^T s(t' + \tau) a(t') \exp[-i2\pi(f_{\text{IF}} + f_{\text{SP}} + \Delta f)t']dt' \\
\Delta f &= j\delta f \ \forall j \in \mathbb{Z} \\
\delta f &= \frac{1}{2T}
\end{aligned}
\tag{1}
$$

where τ is the delay coordinate in GNSS chip units (τ_c); and Δf is the Doppler coordinate, which is referred to the Doppler frequency at the SP (f_{SP}). For both TDS-1 and CYGNSS, Δf is an integer multiple of the Doppler grid spacing δf. The Doppler grid spacing is uniquely related to T, the coherent integration time, through the relationship depicted in (1), in agreement with the Shannon–Nyquist sampling theorem [27]; s is the incoming reflected field; and a is the PRN replica code. The reference time coordinate (t_0) has been omitted in order to simplify the notation, but it is meant for all the terms in (1), namely Y, s, and a. T is equal to 1 ms for both regular TDS-1 and CYGNSS DDMs, leading to a Doppler resolution of 1 kHz and a grid spacing δf equal to 500 Hz. It comes out that, according to the Shannon–Nyquist sampling theorem, the incoming GNSS-R signal is properly sampled and no signal information is lost. Nonetheless, the choice of a Doppler grid spacing smaller than half the Doppler resolution can lead to a more profitable exploitation of the signal. When the Doppler grid spacing is equal to the minimum required value, some distortions of the signal may occur and a proper signal reconstruction could be advised.

In this version of (1), we have explicitly stated that the Doppler frequency at the exponent is the sum of the "intermediate frequency" (f_{IF}), f_{SP}, and the Doppler coordinate of Y. Δf spans in the range $\pm f_{\text{MAX}}$, namely ± 5 kHz for the "full" version of the DDM and ± 2.5 kHz for regular CYGNSS DDMs. When the incoming GNSS reflected signal enters the receiver antenna, its $L1$-band carrier frequency is transformed to f_{IF}, which is more suitable for digital processing [28]. Then, the signal is processed by the on-board correlator according to (1).

The correlation integral depicted in (1) is quite similar to the convolution integral, and therefore, they share most of mathematical properties. One of them is that if the frequency value at the exponent is shifted by Δf_{SP}, $|Y|$ does not change, and the same happens to the resulting power ($|Y^2|$, also known as the waveform (WF) at the Doppler coordinate Δf). The consequence of such property is that if the on-board estimate of the SP location ($\hat{f}_{\text{SP}}$) leads to

$$
\hat{f}_{\text{SP}} = f_{\text{SP}} + \Delta f_{\text{SP}}
\tag{2}
$$

with Δf_{SP} being the error, then the resulting DDM will simply be shifted in the Doppler domain with respect to the correct DDM. However, this property holds only if the following condition is met:

$$
\Delta f_{\text{SP}} = k\delta f \quad \forall k \in \mathbb{Z}.
\tag{3}
$$

TABLE II
SYNTHETIC DESCRIPTION OF THE TWO DATASETS USED IN THIS ARTICLE

	DS_1	DS_2
Period/Date	Apr-Jun 2017	25 Aug '17 & 8 Sep '17
Type	Regular	Raw IF
Collocations	ASCAT/OSCAT	N.A.
QC	CYG_{QC}+$SCAT_{QC}$+QC[20]	CYG_{QC}+QC[20]
# of points	3,007,480	2

CYG stands for CYGNSS, QC for quality control, SCAT for both ASCAT and OSCAT scatterometers, whereas QC [20] stands for the QC scheme used in [20]

In other words, it only holds if Δf_{SP} is an integer of the Doppler sampling grid. If this condition is not met, some sampling issues may occur, giving rise to a different distribution of the incoming power across the DDM bins. This feature is demonstrated in Sections III and IV. Considering that Δf_{SP} varies continuously, this could be achieved only for $\delta f \to 0$.

III. DATASET AND METHODOLOGY

As already mentioned in Section I, two different datasets of CYGNSS DDMs have been used in this article. The description of the datasets together with the analysis methodology used for each individual dataset can be found in the following sections. A summary of the two datasets is shown in Table II.

A. Dataset 1

The first dataset (DS_1) consists of a set of CYGNSS measurements acquired during a time period of three months, spanning from April 1, 2017 to June 30, 2017. CYGNSS measurements are freely downloadable from the Physical Oceanography Distributed Active Archive Center FTP site of the Jet Propulsory Laboratory of the U.S. National Aeronautics and Space Administration [29]. These DDMs have then been collocated with the operational 1-h forecast winds from ECMWF NWP output and with the winds derived from the Advanced Scatterometers (ASCAT) A and B, flying, respectively, on-board MetOp A and B satellites, operated by the European Agency for the Exploitation of Meteorological Satellites (EUMETSAT), and from the OceanSat Scatterometer (OSCAT), on-board ScatSat-1, operated by the Indian Space Research Organization [3]. Both scatterometer wind products have a similar spatial resolution of 25 km and similar accuracies, better than 1 ms^{-1} [1], and are freely available from the EUMETSAT Ocean and Sea Ice Satellite Application Facility website [30]. The spatial resolution of CYGNSS level 2 products is also similar to that of scatterometer-derived winds [5]. CYGNSS DDMs and scatterometer winds have been collocated according to the following spatiotemporal criteria: 1) the maximum distance between the CYGNSS SP and the center of the scatterometer wind vector cell is within 25 km; and 2) the time lag between CYGNSS and scatterometer acquisitions is within 20 min. The ECMWF model wind data are quadratically interpolated with respect to time and bilinearly interpolated with respect to the CYGNSS SP [31]. The entire dataset has been quality controlled (QC) according to the scheme depicted in [20]. For the sake of brevity, only the main important aspects of such QC scheme are reported here. Further details can be found in the aforementioned reference. The QC algorithm consists of two steps, both based on cross correlation
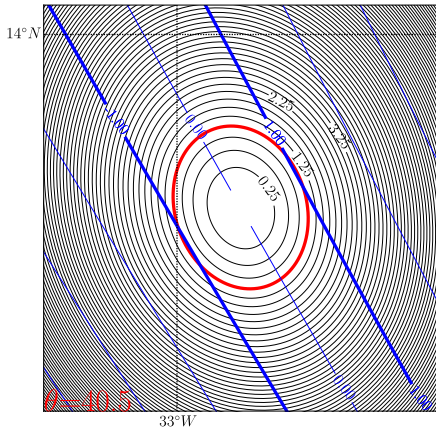
Fig. 1.   Iso-delay (elliptical) and iso-Doppler (straight) lines when the incidence angle at the SP is around $40°$. Thick red line: iso-delay line tangent to the WFs at ± 1 kHz (blue thick lines).
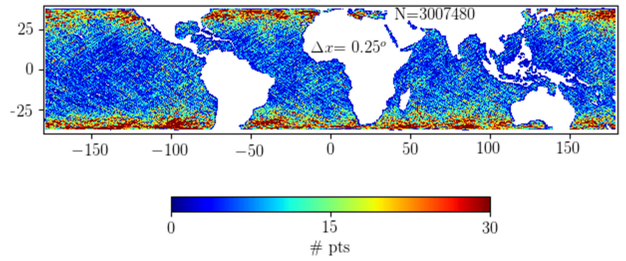

Fig. 2.   Density plot of the dataset 1 (DS_1). The total number of available point after QC is indicated on the plot (N), together with the geographical spatial grid adopted for the latitude–longitude binning (Δx).

functions. The first step consists of cross-correlating the inner core of the measured DDM with the simulated one. Simulated DDMs are computed by means of the WAVeform simulation in PYthon [32], by using ECMWF winds and the acquisition geometry information from CYGNSS metadata. Only the DDMs that well correlate to the simulated ones are retained in the analysis. This test filters out about the 60% of the remaining DDMs after the quality flagging from CYGNSS metadata. The second step consists of assessing the eventual presence of any DDM shape distortions, by evaluating the time lag between the measured normalized WFs at 1 and -1 kHz. Note that the time lag is considered positive (negative) when the WF at 1 kHz is advanced (delayed) with respect to that at -1 kHz. In particular, the second step is used to prove that CYGNSS DDMs suffer from the same distortions as those of TDS-1 DDMs. Only the DDMs with incidence angles at the SP lower than 40° have been retained. If the aforementioned WFs are shifted with respect to each other, it means that the delay–Doppler symmetry is broken and distortions are apparent. The rationale of such assertion is well explained by Fig. 1. Here, the red elliptical line represents the iso-delay line tangent to both iso-Doppler lines at ± 1 kHz. This is to say that the arrival time of these two WFs should be identical, underlining that the eventual presence of any delay shift is attributable to a distorting effect. Actually, this delay–Doppler symmetry is kept for incidence angles up to $60°$ for CYGNSS orbital features. Nonetheless, at such high values of the incidence angle, the signal-to-noise ratio is not as favorable as for lower incidence angles. The eventual occurring shift caused by the local geophysical conditions is accounted for through the simulated DDM as explained in [20]. Indeed, the presence, for example, of strong wind gradients may affect such test if not properly taken into account. Finally, the entire dataset has been flagged according the quality flags of both CYGNSS and scatterometer winds. The entire QC-passed dataset consists of 3 007 480 DDM-scatterometer wind-ECMWF wind triplets. Fig. 2 shows a density plot of the CYGNSS SP locations of DS_1.

The receiver antenna gain pattern variations across the glistening zone do affect the received power levels. A proper calibration of the bin by bin DDM σ_0 should take this into account. In

order to assess the sensitivity of the analysis shown in this article to such effects, the estimated relative shift between the normalized WFs has been evaluated by taking into account also the projection of the antenna gain pattern on the WFs at ± 1 kHz.

In addition, it is worth to analyze the sensitivity of relative WF shifts with respect to the incidence angle. For such purpose, the trend of the relative WF shifts with respect to the Doppler frequency error at the SP has been analyzed for four incidence angle intervals spanning from $20°$ to $40°$, each $5°$ wide.

B. Dataset 2

The second dataset (DS_2) consists of two 60-s tracks of raw IF CYGNSS data over hurricanes Harvey and Irma, which made landfall on the U.S. coasts during summer 2017. Harvey's track has been acquired on 25 August, whereas Irma's on 8 September. Such kind of CYGNSS data are not routinely downloaded to the ground segment, and are available only for scientific purposes. They are occasionally acquired in special circumstances, such as extreme events and can be accessed under request to the responsible of the CYGNSS scientific mission, Dr. C. Ruf. Note that there is no special reason to use hurricane cases for this analysis. However, raw data are only available under such conditions. Consequently, the results shown in the course of this article do not depend on the specific geophysical scene but only on SP inaccuracies. The reason for choosing two different cases is that in Harvey's case, Δf_{SP} is one order of magnitude higher than in Irma's case. The comparison of WFs at ± 1 kHz can immediately give a perception of such distortions, as shown later in Section IV (see Fig. 8). For the sake of reproducibility, Figs. 3 and 4 show a synoptic view of both hurricanes on the reported dates, together with the CYGNSS raw IF tracks used for the analysis proposed here (depicted in red).

Only the 1-s (the incoherent integration time) raw IF data slots corresponding to good quality regular DDMs have been considered for this analysis. They amount to 56 for Harvey and 33 for Irma. Raw IF data are recompressed by varying f_{SP} in the range $[f_{SP} - 250$ Hz $, f_{SP} + 250$ Hz$]$ in steps of approximately 35 Hz, not evenly spaced, aiming at sampling the entire DDM Doppler grid spacing of 500 Hz. This way, the gradual modifications of the recompressed DDM can be appreciated, and the periodicity of the convolution integral depicted in (1) for Δf_{SP} equal to δf can be verified. Raw IF data are recompressed by means of the raw IF processor available for scientific purposes in the context of the CYGNSS science team,
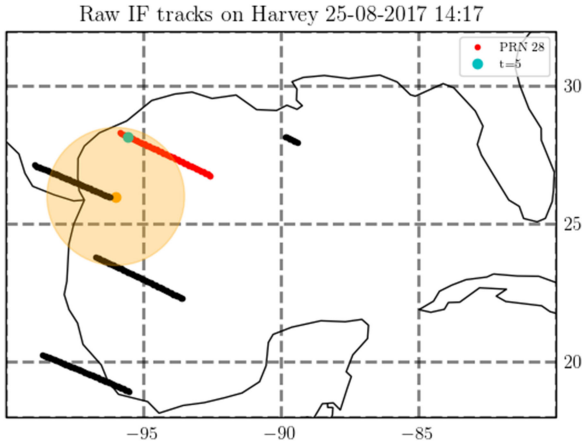
Fig. 3. Orange patch shows the inner core of hurricane Harvey on 25 August at 14:17 UTC. The red track represents the selected CYGNSS track for the recompression of raw IF data at the same time. The cyan bullet represents the location of the DDM at time $t = 5$ s used in this analysis.
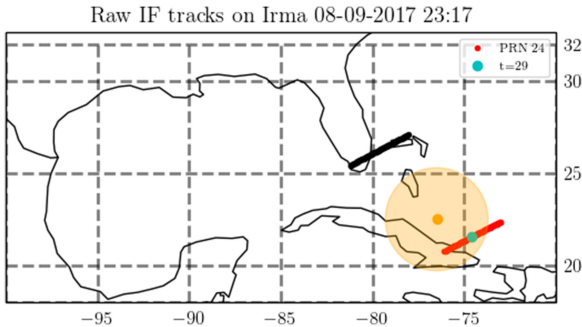

Fig. 4. Orange patch shows the inner core of hurricane Irma on 8 September at 22:15 UTC time. The red track represents the selected CYGNSS track for the recompression of raw IF data 1 h later. The cyan bullet represents the location of the DDM at time $t = 29$ s used in this analysis.

and provided by Dr. S. Gleason. It implements the correlator integral of (1). Several parameters can be input in this processor, among f_{SP}. It is important to remark that the original software implemented on-board CYGNSS is not open source and has not been made available by SSTL. The thorough comparison of such recompressed DDMs with their corresponding regular DDMs is not within the scope of this article. We report here that regular and recompressed DDMs with the same on-board parameters have some nonnegligible differences, which may be attributable to an eventual finer on-board filtering that is not implemented in the raw processor used here (personal communication with Dr. S. Gleason). For illustrative purposes, Fig. 5 shows the regular DDM acquired on Harvey's selected track (Fig. 5(a), cyan point) and that obtained by recompressing the raw IF signal with the same on-board $\hat{f}_{SP}$. The latter is reported in the white legend of the mentioned figure, together with f_{SP}. It is evident that despite the main features of the regular DDM are reasonably reproduced in the recompressed DDM, differences are apparent. In particular, the intensity of the regular DDM peak is higher than the recompressed one and, in general, the intensity of the DDM horse shoe is higher in the regular DDM than in the recompressed DDM. Instead, if one looks at the external part of

the DDM horse shoe, which is supposed to represent the noise floor, actually there is a "halo." This seems to suggest that the recompressed DDM is more blurred with respect to the regular DDM, indicating a higher spreading of the signal energy over the surrounding delay–Doppler bins.

For the analysis presented in this article, the raw IF processor used here is enough accurate and reliable. It is worth to remark that regular DDMs are not used for this analysis. Therefore, the recompressed DDMs according to the mentioned procedure are all consistent with each other. One of the input parameters of the raw processor is f_{IF} [see (1)]. The value of f_{IF} provided by SSTL is 3 872 400 Hz (personal communication with Dr. Gleason). It has been verified that, by using this value, the recompressed DDMs are systematically shifted toward negative Doppler values. This feature is compatible with an overestimation of the exponent of (1). Assuming that the *a posteriori* value of f_{SP} provided in the CYGNSS data product is correct, then the f_{IF} is overestimated. Based on the fact that WFs at ±1 kHz should have the same arrival time (see Fig. 1 and related discussion in Section III-A), a rough trial and error procedure for f_{IF} estimation leads to the value of 3 872 180 Hz. Probably, this value could be finer tuned, but this is beyond the scope of this article. As such, the aforementioned estimated f_{IF} value is used in this analysis.

IV. RESULTS

Fig. 6(a) shows a density contour plot of the relative shifts of the normalized WFs at ±1 kHz ($\Delta\tau$ on the *y*-axis) versus the error of the Doppler frequency at the SP (Δf_{SP} on the *x*-axis), evaluated according to (4), for DS_1. Δf_{SP} is defined according to (4), where $\hat{f_{SP}}$ is the on-board estimation of the Doppler frequency at the SP and f_{SP} is the *a posteriori* estimation based on a geoid model of the earth. The dashed magenta line is the corresponding fitting curve. Some additional information, such as the correlation coefficient (r), the slope and intercept of the curve (a and b, respectively), and the probability associated to the null test (p), are reported on the plot. The color bar labels represent the percentiles (in the range 0–1) of the entire dataset. For the sake of comparison, [20, Fig. 9] is reported in Fig. 6(b), by using the same definitions stated before, the same coloring and the same axis ranges, and by reporting the same diagnostic information:

$$\Delta f_{SP} = \hat{f_{SP}} - f_{SP}. \tag{4}$$

By comparing Fig. 6(a) and (b), several common features are evident, but also some important differences. A thorough discussion about the differences between CYGNSS and TDS-1 is beyond the scope of this article. Hereafter, only a few major aspects related to the analysis presented in this article will be discussed. First, it is evident that the distorting mechanism induced by the SP inaccuracies is common to both missions. It is important to remark that both CYGNSS and TDS-1 share the SGR-ReSI instrument and, therefore, the same algorithm for the fast computation of the SP location [21]. The correlation coefficient (r) between $\Delta\tau$ and Δf_{SP} is higher for TDS-1 than for CYGNSS, even if both are significant. It is also evident that both $\Delta\tau$ and Δf_{SP} ranges are different for the two missions. The
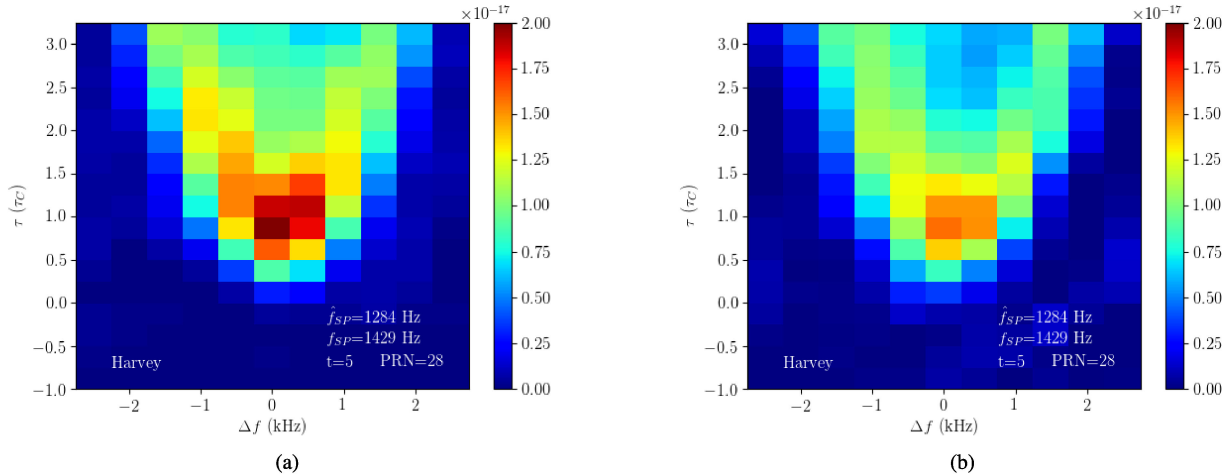
Fig. 5. (a) Regular DDM acquired on Harvey's track at instant of time $t = 5$ s. (b) Recompressed DDM with the same on orbit parameters.
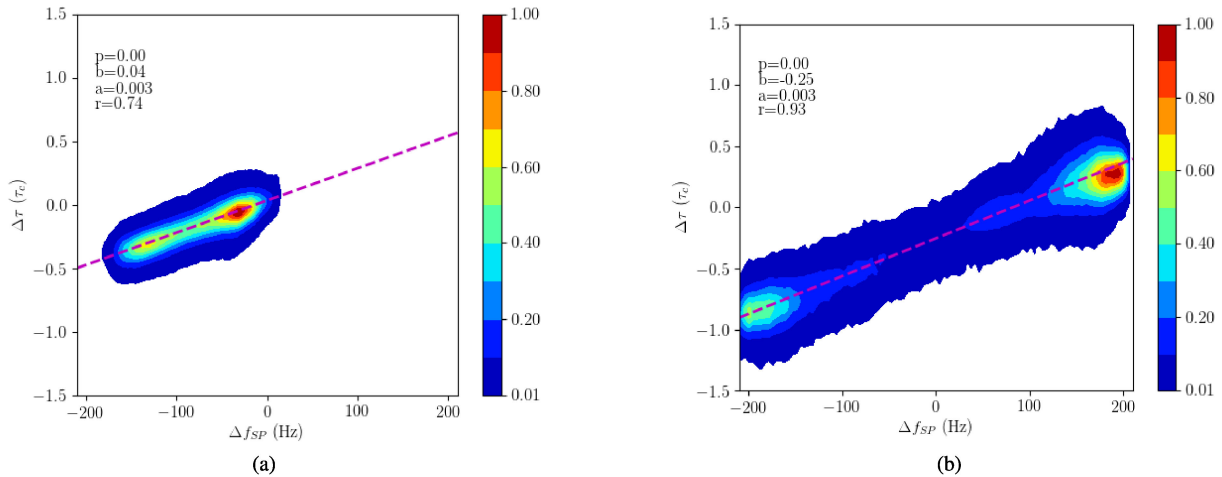

Fig. 6. (a) Density plot of the relative shifts of the normalized WFs at ± 1 kHz ($\Delta\tau$) versus the Doppler frequency error at the SP (Δf_{SP}), evaluated on DS$_1$. (b) Same as (a) but for the TDS-1 dataset used in [20].

wider Δf_{SP} range for TDS-1 with respect to CYGNSS may lead to a higher correlation coefficient between Δf_{SP} and $\Delta\tau$. These range differences are most likely due to the different orbital features. Indeed, as said before, TDS-1 lies on a polar orbit, at about 800 km of altitude, whereas CYGNSS receivers lie on a 35° inclined orbit over the equator, at about 530 km of altitude. We believe that such distortions are strongly modulated by the orbital features. Another clue that alleges such assertion is that both distributions are bimodal, peaking toward the extremes of the ranges. In fact, while the CYGNSS Δf_{SP} distribution peaks at approximately -20 Hz (main peak) and at -130 Hz (secondary peak), the TDS-1 one peaks at ± 200 Hz. Both $\Delta\tau$ distributions reflect the same features. Fig. 7 can help to better understand such allegation. Fig. 7(a) and (b) show the geographical distribution of Δf_{SP} for the CYGNSS (TDS-1) descending tracks of the DS$_1$ dataset (TDS-1 dataset of [20]). From Fig. 7(a) and (b), it can be seen that the absolute value of Δf_{SP} increases polewards reaching its maximum at approximately $\pm 25°$ ($\pm 50°$) before descending again in the same direction. It is apparent that Δf_{SP}

is modulated by the different elevation of the receivers. The corresponding maps for ascending tracks show similar patterns but the sign of Δf_{SP} is reversed.

In [20], it has been verified that both distributions peak slightly before the aphelion and the perihelion. Finally, the slope of the fitting curves is identical for both missions.

If the antenna gain pattern corrections are taken into account for CYGNSS, the results are not significantly different. Indeed, the differences between the slopes of $\Delta\tau$ versus Δf_{SP} happen at the third significant digit, and the same happens both for the intercept and the correlation coefficients (not shown).

On the other hand, a slight steady increase of the slope with respect to the incidence angle can be seen in Table III. The value of the slope for the incidence angle bin between 20° and 25° is equivalent to one delay bin for $\Delta f_{SP} = 100$ Hz, increasing by more than 10% for incidence angles between 35° and 40°.

Fig. 8(a) and (b) show the normalized WFs at ± 1 kHz in solid and dashed lines, respectively, at the acquisition instant of time $t = 5$ s ($t = 29$ s) of Harvey's (Irma's) selected track. Some
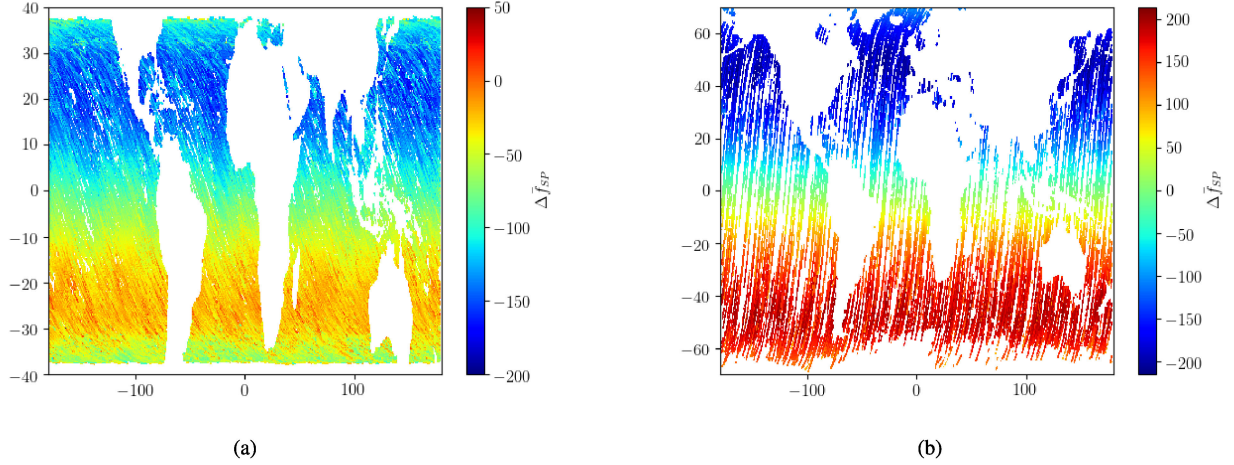
Fig. 7. (a) Geographical distribution of Δf_{SP} for CYGNSS descending tracks. (b) Same as (a) but for the TDS-1 dataset used in [20].
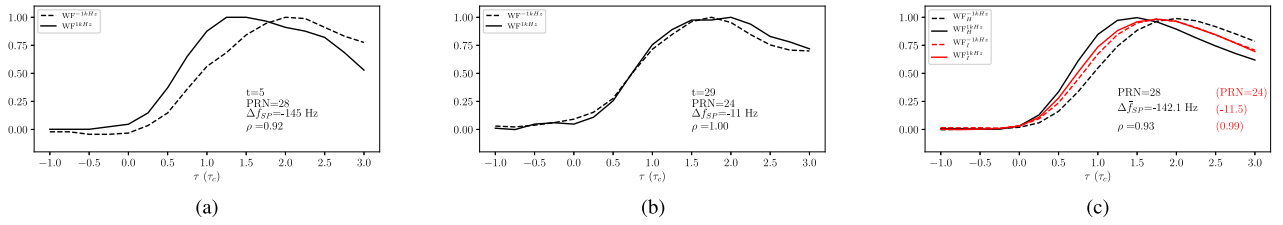

Fig. 8. (a) Normalized WFs at ± 1 kHz, in solid and dashed lines, respectively, for Harvey's track. t is the instant of time of acquisition; PRN is the GPS transmitter; Δf_{SP} is the error on f_{SP}; ρ is the cross correlation between the two WFs. (b) Same as (a) but for Irma. (c) Averaged WFs for Harvey (Irma) in black (red) along the entire track.

TABLE III
SENSITIVITY OF $\Delta \tau$ W.R.T. THE INCIDENCE ANGLE AT THE SP (θ)

θ	a	$\Delta \tau_{100}$
20°-25°	2.5e-3	0.25
25°-30°	2.6e-3	0.26
30°-35°	2.7e-3	0.27
35°-40°	2.8e-3	0.28

a is the slope of the fitting curve.
$\Delta \tau_{100}$ is the equivalent $\Delta \tau$ for $\Delta f_{SP} = 100$ Hz.

ancillary information is reported on the plot, such as the PRN of the GPS transmitter, the value of Δf_{SP} and the cross correlation coefficient of the two WFs. It is evident that for Harvey's track, WFs are shifted with respect to each other, clearly evidencing that the arrival time is different. The shift amounts approximately to 0.5 τ_c, which corresponds to two delay bins. This result is consistent with Fig. 6(a). However, the shift is not apparent on Irma's track. This feature is constant for both entire tracks and is clearly related to Δf_{SP}. The higher $|\Delta f_{SP}|$, the larger the shift. Fig. 8(c) shows the averaged normalized WFs at ± 1 kHz (solid and dashed, respectively) for Harvey's and Irma's tracks in black and red, respectively. It can be easily appreciated that Irma's WFs are closer to each other than Harvey's WFs. Furthermore, it is evident that Harvey's WF at 1 kHz is steeper than both Irma's WFs, which are, in turn, steeper than Harvey's WF at -1 kHz. This seems to suggest that some LESs are affected

by the sampling problems discussed in Section II and some others not. In the following paragraphs, we link the sampling issues to the presence (absence) of shifts on Harvey's (Irma's) DDMs.

Fig. 9(a) shows the recompressed DDM at the instant of time $t = 5$ s of Harvey's track [same as Fig. 5(a)], with the value of $\hat{f}_{SP}$ as written on the plot. In Fig. 9(b), the raw incoming signal has been recompressed with $\hat{f}_{SP}$ higher than in Fig. 9(a) by 500 Hz. It can be seen that the two DDMs are identical, but that in Fig. 9(b) is one Doppler bin shifted toward negative values with respect to Fig. 9(a). If we shift one of the two DDMs in order to overlap the other, the difference is exactly zero. Such plot is not shown for the sake of brevity. This example proves that if the constraint depicted in (3) is matched, the correlation integral in (1) is invariant with Δf_{SP}.

Fig. 10 shows the recompressed normalized WFs at ± 1 kHz (solid and dashed lines, respectively) at the instant of time equal to 5 s of Harvey's track, obtained with five different values of Δf_{SP} in the range $[-250, 250]$ Hz, among which, one corresponds to the on-board estimation $\hat{f}_{SP}$ [see Fig. 10(b)] and one to the *a posteriori* estimation f_{SP} [see Fig. 10(c)]. ρ is the cross correlation coefficient value of the WFs. It can be seen that the lower the $|\Delta f_{SP}|$, the more the WFs tend to overlap. This trend is confirmed also by the cross correlation coefficient, which reaches its maximum when Δf_{SP} is equal to 0 Hz. This is the demonstration that some sampling issues are caused by SP inaccuracies.
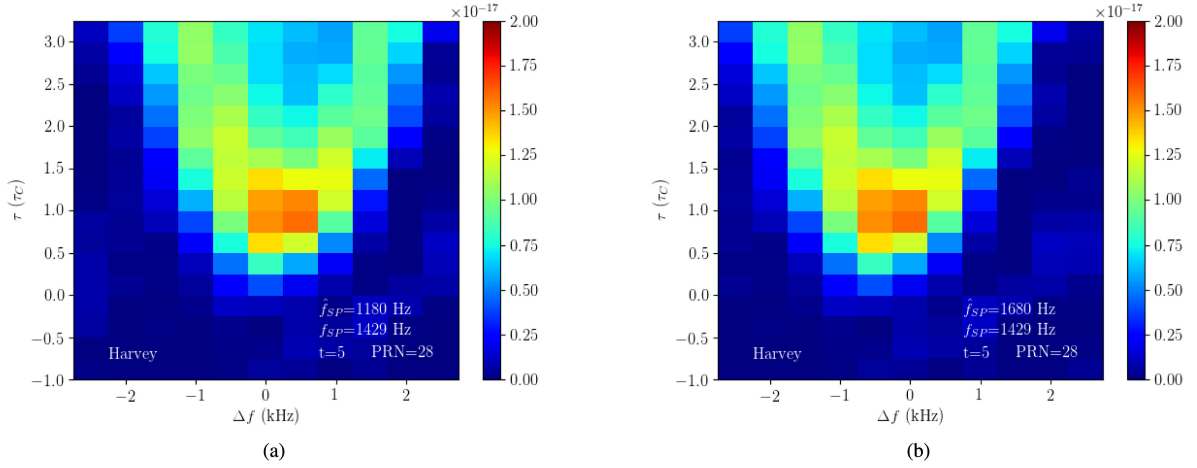
Fig. 9. (a) Recompressed DDM with the value of $\hat{f}_{SP}$ indicated on the plot. (b) Same as (a) but that $\hat{f}_{SP}$ is 500 Hz larger. Note that besides the shift, bin values are identical within the roundoff machine error.
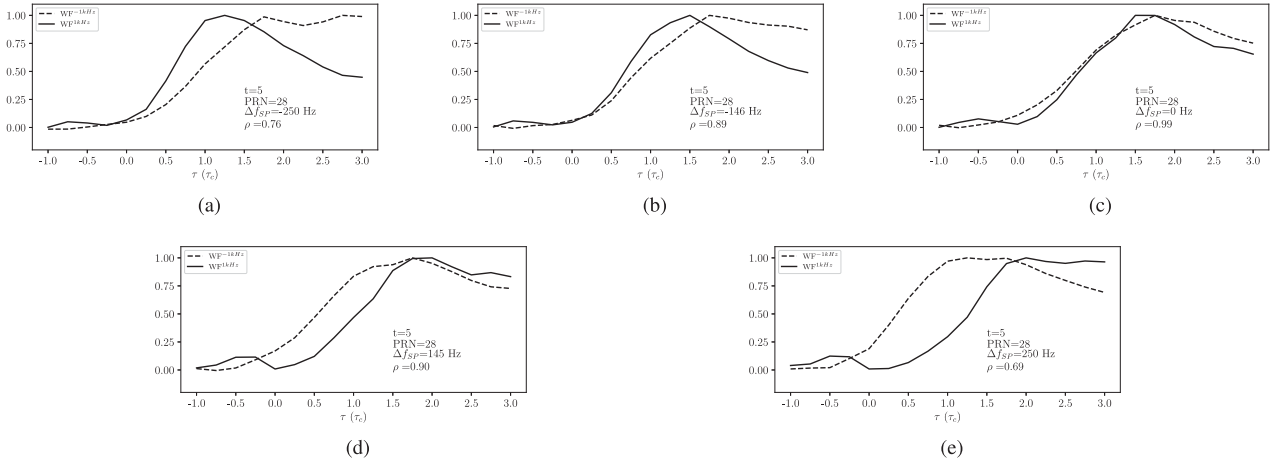

Fig. 10. Normalized WFs at ±1 kHz (solid and dashed lines, respectively) for the value of Δf_{SP} indicated in each plot, at the instant of time equal to 5 s of Harvey's track. ρ is the cross correlation coefficient value of the WFs.

A quite simple way to overcome such SP induced distortions is to oversample the DDM during the correlation procedure, before downloading it to the ground segment. Indeed, if δf would be n times smaller than it is at the moment (500 Hz), $\forall n \in \mathbb{N}$, the size of the outcoming DDM would be n times larger, along the Doppler dimension (this quantity is referred to as δf_n here on). If, for example, $n = 10$, $\delta f_n = 50$ Hz and the outcoming DDM shape would be 101×17 instead of 11×17, as it is at the moment for CYGNSS. As the correlation procedure is channel-by-channel independent in the Doppler dimension, the most accurate DDM would simply be a downsample of the DDM (1 Doppler channel every 10), by taking into account the apt Doppler lag (l_D). l_D can be retrieved from the following formula:

$$l_D = -\operatorname{sgn}(\Delta f_{SP}) \left\{ \left\lfloor \frac{|\Delta f_{SP}| - \frac{\delta f_n}{2}}{\delta f_n} \right\rfloor + 1 \right\}$$

$$\delta f_n = \frac{\delta f}{n} \qquad (5)$$

where $\operatorname{sgn}(\cdot)$ and $\lfloor \cdot \rfloor$ are the signum and the floor functions, respectively. If Δf_{SP} is around -145 Hz (as for the case of Harvey's track presented here), l_D equals to 3. This way, $|\Delta f_{SP}|$ is reduced to 5 Hz, and, in general, its maximum value amounts to 25 Hz, which is quite reasonable. Of course, the other side of the coin is that the data bulk to be downloaded would be n times larger. Fig. 11 can help to better understand the idea behind this strategy. Fig. 11(a) represents the DDM obtained with the on-board estimation $\hat{f}_{SP}$, for Harvey's track, at the instant of time value equal to 5 s, with $\delta f_n = 50$ Hz. The red strips represent the Doppler channels corresponding to the regular CYGNSS DDM, as computed onboard, from which the DDM in Fig. 5(b) is obtained. The green strips are the Doppler channels corresponding to the closest value of $\hat{f}_{SP}$ to the *a posteriori* estimate of f_{SP} (their difference is only 5 Hz). The resulting DDM is shown in Fig. 11(b). By comparing Figs. 5(b) and 11(b), it can be seen that the shape of the horse shoe is now more symmetrical and the peak intensity is higher in the latter. Furthermore, it seems that the energy around the
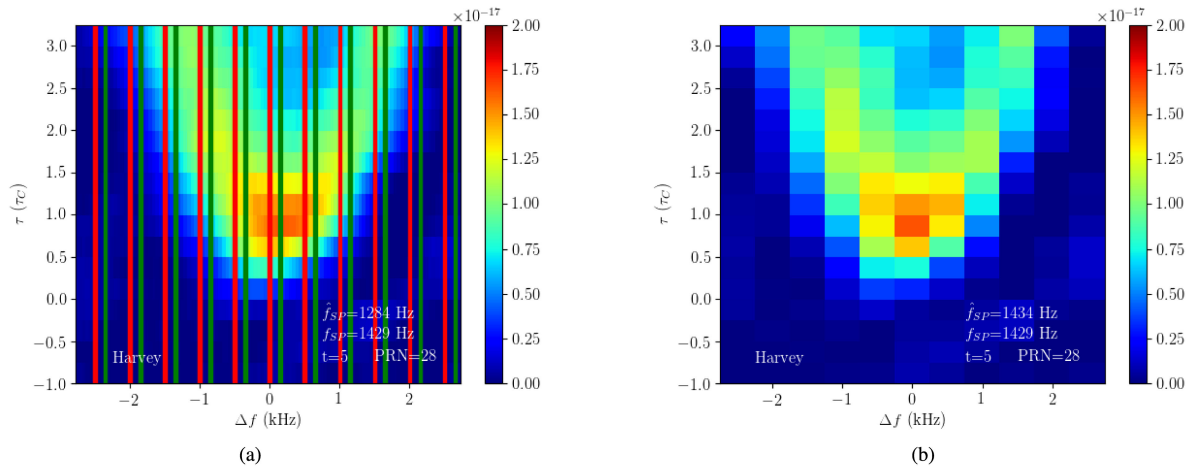
Fig. 11. (a) Oversampled DDM with $\delta f_n = 50$ Hz and the on-board estimation of f_{SP}, for Harvey's track at $t = 5$ s. Red strips: Doppler channels location relative to the on-board DDM. Green strips: Doppler channels location relative to the closest $\hat{f}_{SP}$ (1434 Hz) on the new oversampled Doppler grid. (b) DDM corresponding to the green strips.

peak is more concentrated in the peak than in the surrounding bins in Fig. 11(b).

An alternative approach consists on reconstructing the DDM from the possibly distorted one. Indeed, the GNSS-R signal is properly sampled according to the Shannon–Nyquist theorem, therefore, no signal information is lost in the DDM compression procedure. This attempt is left for future studies.

V. DISCUSSION

In this article, a thorough analysis of the CYGNSS DDM distortions induced by SP inaccuracies has been carried out. A dataset of three months has been analyzed, confirming that CYGNSS DDMs present the same kind of distortions as TDS-1 DDMs. Such distortions may lead to relative shifts of the WFs at ± 1 kHz amounting to $0.5\tau_c$ (two delay bins). This value is lower than that of TDS-1 DDMs, most likely because of the different orbital features of the two missions. Such aspect needs to be further investigated. The rationale of such distorting mechanism has been revealed by analyzing two raw IF data tracks over hurricanes Harvey and Irma, which made landfall on U.S. coasts during summer 2017. The SP inaccuracies present in these two tracks are one order of magnitude different, being higher for Harvey. It turns out that Harvey's DDMs are more distorted than those of Irma, confirming the results from the three months dataset. Therefore, the higher the SP inaccuracies, the higher the distortions. It has been demonstrated that SP induced distortions dramatically reduce by recompressing the raw incoming signals with more accurate estimates of the Doppler frequency at the SP. This aspect clearly shows that SP inaccuracies induce some sampling issues. Such distortions may even affect the LES of the WFs around the SP, and therefore can impact the so-called LES observable used for wind retrievals in the operational CYGNSS processor. Furthermore, all multilook retrieval approaches aiming at exploiting the DDM ambiguity-free zone may be strongly compromised by such distortions. How much operational CYGNSS observables and

the aforementioned retrieval approaches may be affected by such distortions is a topic for future investigations.

However, in order to have an idea of the potential impact of these distortions on the wind speed retrieval, a very simple analysis is proposed here. Fig. 12(a) shows the deviations of the CYGNSS operational observable DDMA (σ_0) with respect to the average value for May 2017 in the entire range of Δf_{SP}. Four different 1 ms^{-1} wide wind speed bins around 1.5, 9.5, 12.5, and 15.5 ms^{-1} have been analyzed, in order to more thoroughly assess the impact of such distortions on the wind speed retrieval. The projection of these errors on the retrieval is reported at the bottom right corner of each plot. Fig. 12(b) shows the same deviations as Fig. 12(a) but with respect to the error in delay fraction at the SP ($\Delta\tau_{SP}$). The plots suggest that these errors can represent 25% of the wind speed retrieval values.

A simplistic approach for assessing such effects on the wind speed retrieval has been used. As already mentioned, a more thorough analysis, which is beyond the scope of this article, is needed to better characterize these errors. Nonetheless, the reported scores suggest that these effects are not negligible.

Such kind of inaccuracies may also severely impact altimetric applications if not properly taken into account. In order to have an estimation of their impact, the point of maximum leading edge derivative has been assessed for both normalized WFs at 0 Hz obtained by convolving the raw signal with the on-board estimation of f_{SP} and its most accurate estimate, for the same case depicted in Fig. 5(b) [33]. The difference between these two points has been projected on the vertical direction. The estimated sea surface height (SSH) retrieval error is around 6 m.

A quite straightforward solution to this problem could be that of uploading the predicted SP locations obtained by combining the *a priori* information on future satellite position and an accurate geoid model. At the moment, such solution is not feasible for CYGNSS (personal communication with C. Ruf), but could be considered for future missions.

A simple strategy aiming at limiting such distortions by keeping the computational efficiency of the QS approximation
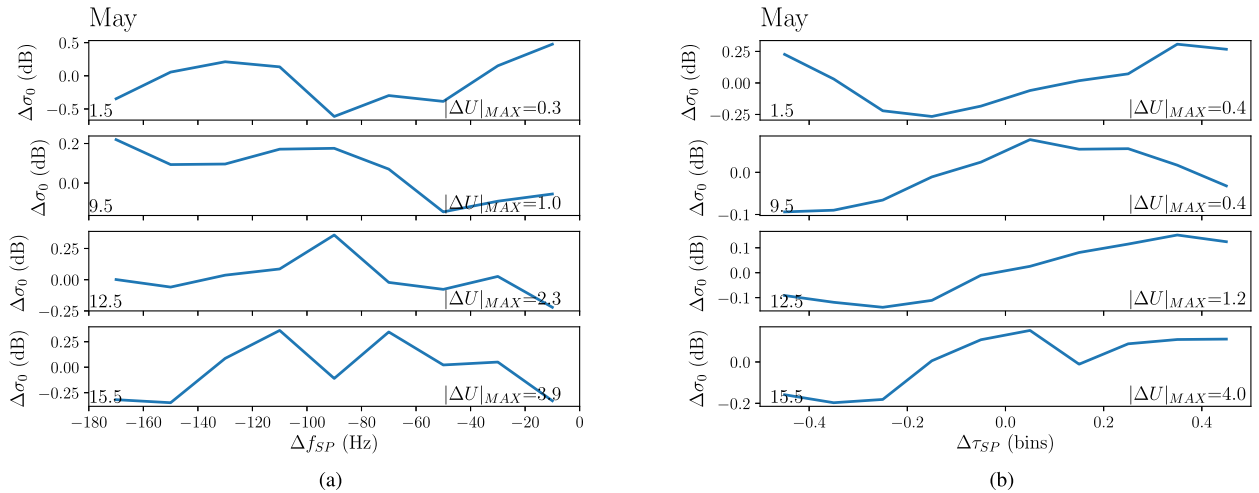
Fig. 12.   (a) σ_0 deviations with respect to the average value of σ_0 for the entire period of May 2017, and for four different wind speed bins. The deviations are plotted versus Δf_{SP}. The central value of the wind speed bin is reported at the bottom left corner of each plot, whereas the maximum impact on the wind speed retrieval is reported at the right bottom corner. (b) Same as (a) but σ_0 deviations are plotted versus errors in delay at the SP.

has been proposed. It consists of oversampling the on-board DDM, by reducing the Doppler grid spacing by a factor 10. This way, an optimal subsample of the DDM could be chosen *a posteriori*, leading to a maximum Doppler frequency inaccuracy at the SP of 25 Hz, an order of magnitude higher than the current accuracy. It is important to remark that, according to the density plot shown in Fig. 6(a), factor 10 suggested here could be useful to effectively reduce the relative WFs shifts, with a supposed positive impact on multilook approached aiming at exploiting the DDM horse shoe. The impact of such choice on the accuracy of the routine DDM observables is not yet assessed. Such aspect is demanded for future work.

An alternative approach consists on *a posteriori* reconstructing the DDM. Indeed, the GNSS-R signal is properly sampled according to the Shannon–Nyquist theorem and no signal information is lost. This approach is left for future studies.

VI. Conclusion

The rationale of GNSS reflected DDM distortions, induced by specular point inaccuracies, is investigated through extensive analysis. Such distortions may lead to a relative shift of the WFs at ± 1 kHz amounting to two delay bins. This means that the map of the entire free of ambiguity zone onto the DDM is distorted, hampering the exploitation of all bins for wind speed retrieval.

Even if a detailed analysis of the impact of such distortions on the routine CYGNSS observables is postponed to future studies, some preliminary evaluations show that they could lead to errors in the order of 25% on the wind speed retrievals. In the same way, the SSH retrieval accuracy may be affected by such distortions, with an error in the order of several meters. A few effective strategies aiming at reducing such distortions are proposed.

Although not tested, the same approaches could be used with TDS-1 DDMs since both CYGNSS and TDS-1 share the same instrument (SGR-ReSI) and the same QS approximation algorithm for the on-board computation of the SP.

Finally, for future GNSS-R missions, raw data storing is recommended for eventual reprocessing in case of miscalibration or processing issues such as those demonstrated here.

References

[1] A. Stoffelen, J. A. Verspeek, J. Vogelzang, and A. Verhoef, "The CMOD7 geophysical model function for ASCAT and ERS wind retrievals," *IEEE J. Sel. Topics Appl. Earth Observ. Remote Sens.*, vol. 10, no. 5, pp. 2123–2134, May 2017.

[2] A. Stoffelen *et al.*, "Research and development in Europe on global application of the OceanSat-2 scatterometer winds," KNMI-NWP SAF-OSI SAF, De Bilt, The Netherlands, Tech. Rep. NWPSAF-KN-TR-022-SAF/OSI/CDOP2/KNMI/TEC/RP/196, May 2013. [Online]. Available: https://www.nwpsaf.eu/publications/tech_reports/nwpsaf-kn-tr-022.pdf?e%6316e&e6316e

[3] WMO OSCAR database, 2017. [Online]. Available: https://www.wmo-sat.info/oscar/

[4] M. Unwin, P. Jales, J. Tye, C. Gommenginger, G. Foti, and J. Rosello, "Spaceborne GNSS-reflectometry on TechDemoSat-1: Early mission operations and exploitation," *IEEE J. Sel. Topics Appl. Earth Observ. Remote Sens.*, vol. 9, no. 10, pp. 4525–4539, Oct. 2016.

[5] C. S. Ruf *et al.*, "New ocean winds satellite mission to probe hurricanes and tropical convection," *Bull. Amer. Meteorol. Soc.*, vol. 97, no. 3, pp. 385–395, 2016. [Online]. Available: https://doi.org/10.1175/BAMS-D-14-00218.1

[6] S. M. Leidner, B. Annane, B. McNoldy, R. Hoffman, and R. Atlas, "Variational analysis of simulated ocean surface winds from the cyclone global navigation satellite system (CYGNSS) and evaluation using a regional OSSE," *J. Atmos. Ocean. Technol.*, vol. 35, no. 8, pp. 1571–1584, 2018. [Online]. Available: https://doi.org/10.1175/JTECH-D-17-0136.1

[7] B. Annane, B. McNoldy, S. M. Leidner, R. Hoffman, R. Atlas, and S. J. Majumdar, "A study of the HWRF analysis and forecast impact of realistically simulated CYGNSS observations assimilated as scalar wind speeds and as VAM wind vectors," *Monthly Weather Rev.*, vol. 146, no. 7, pp. 2221–2236, 2018. [Online]. Available: https://doi.org/10.1175/MWR-D-17-0240.1

[8] Y. Krien *et al.*, "Can we improve parametric cyclonic wind fields using recent satellite remote sensing data?" *Remote Sens.*, vol. 10, no. 12, 2018, Art. no. 1963.

[9] S. Zhang, Z. Pu, D. J. Posselt, and R. Atlas, "Impact of CYGNSS ocean surface wind speeds on numerical simulations of a hurricane in observing system simulation experiments," *J. Atmos. Ocean. Technol.*, vol. 34, no. 2, pp. 375–383, 2017. [Online]. Available: https://doi.org/10.1175/JTECH-D-16-0144.1

[10] Z. Cui, Z. Pu, V. Tallapragada, R. Atlas, and C. S. Ruf, "A preliminary impact study of CYGNSS ocean surface wind speeds on numerical simulations of hurricanes," *Geophys. Res. Lett.*, vol. 46, no. 5, pp. 2984–2992, 2019. [Online]. Available: https://agupubs.onlinelibrary.wiley.com/doi/abs/10.1029/2019GL082236

[11] J. Park, J. T. Johnson, Y. Yi, and A. J. OBrien, "Using rapid revisit CYGNSS wind speed measurements to detect convective activity," *IEEE J. Sel. Topics Appl. Earth Observ. Remote Sens.*, vol. 12, no. 1, pp. 98–106, Jan. 2019.

[12] C. S. Ruf and R. Balasubramaniam, "Development of the CYGNSS geophysical model function for wind speed," *IEEE J. Sel. Topics Appl. Earth Observ. Remote Sens.*, vol. 12, no. 1, pp. 66–77, Jan. 2019.

[13] G. Foti *et al.*, "Spaceborne GNSS reflectometry for ocean winds: First results from the UK TechDemoSat-1 mission," *Geophys. Res. Lett.*, vol. 42, no. 13, pp. 5435–5441, 2015. [Online]. Available: https://agupubs.onlinelibrary.wiley.com/doi/abs/10.1002/2015GL064204

[14] F. Said, Z. Jelenak, P. S. Chang, and S. Soisuvarn, "An assessment of CYGNSS normalized bistatic radar cross section calibration," *IEEE J. Sel. Topics Appl. Earth Observ. Remote Sens.*, vol. 12, no. 1, pp. 50–65, Jan. 2019.

[15] S. Gleason, C. S. Ruf, A. J. O'Brien, and D. S. McKague, "The CYGNSS level 1 calibration algorithm and error analysis based on on-orbit measurements," *IEEE J. Sel. Topics Appl. Earth Observ. Remote Sens.*, vol. 12, no. 1, pp. 37–49, Jan. 2019.

[16] T. Wang, C. S. Ruf, B. Block, D. S. McKague, and S. Gleason, "Design and performance of a GPS constellation power monitor system for improved CYGNSS L1B calibration," *IEEE J. Sel. Topics Appl. Earth Observ. Remote Sens.*, vol. 12, no. 1, pp. 26–36, Jan. 2019.

[17] W. Lin, M. Portabella, G. Foti, A. Stoffelen, C. Gommenginger, and Y. He, "Toward the generation of a wind geophysical model function for spaceborne GNSS-R," *IEEE Trans. Geosci. Remote Sens.*, vol. 57, no. 2, pp. 655–666, Feb. 2019.

[18] F. Wang, D. Yang, and B. Zhang, "Geometric distortion correction of spaceborne GNSS-R delay-Doppler map using reconstruction," *IEEE Geosci. Remote Sens. Lett.*, vol. 15, no. 12, pp. 1852–1856, Dec. 2018.

[19] W. Li, E. Cardellach, F. Fabra, S. Rib, and A. Rius, "Effects of PRN-dependent ACF deviations on GNSS-R wind speed retrieval," *IEEE Geosci. Remote Sens. Lett.*, vol. 16, no. 3, pp. 327–331, Mar. 2019.

[20] G. Grieco, A. Stoffelen, M. Portabella, M. B. Rivas, W. Lin, and F. Fabra, "Quality control of delay-doppler maps for stare processing," *IEEE Trans. Geosci. Remote Sens.*, vol. 57, no. 5, pp. 2990–3000, May 2019.

[21] P. Jales, "Spaceborne receiver design for scatterometric GNSS reflectometry," Ph.D. dissertation, Faculty Eng. Phys. Sci., Univ. Surrey, Guildford, U.K., 2012. [Online]. Available: http://epubs.surrey.ac.uk/807880/

[22] J. Tye, P. Jales, M. Unwin, and C. Underwood, "The first application of stare processing to retrieve mean square slope using the SGR-ReSI GNSS-R experiment on TDS-1," *IEEE J. Sel. Topics Appl. Earth Observ. Remote Sens.*, vol. 9, no. 10, pp. 4669–4677, Oct. 2016.

[23] M. P. Clarizia, C. S. Ruf, P. Jales, and C. Gommenginger, "Spaceborne GNSS-R minimum variance wind speed estimator," *IEEE Trans. Geosci. Remote Sens.*, vol. 52, no. 11, pp. 6829–6843, Nov. 2014.

[24] G. Giangregorio, P. Addabbo, C. Galdi, and M. di Bisceglie, "Ocean wind speed estimation from the GNSS scattered power function volume," *IEEE J. Sel. Topics Appl. Earth Observ. Remote Sens.*, vol. 12, no. 1, pp. 78–86, Jan. 2019.

[25] N. Rodriguez-Alvarez and J. L. Garrison, "Generalized linear observables for ocean wind retrieval from calibrated GNSS-R delay Doppler maps," *IEEE Trans. Geosci. Remote Sens.*, vol. 54, no. 2, pp. 1142–1155, Feb. 2016.

[26] V. U. Zavorotny and A. G. Voronovich, "Scattering of GPS signals from the ocean with wind remote sensing application," *IEEE Trans. Geosci. Remote Sens.*, vol. 38, no. 2, pp. 951–964, Mar. 2000.

[27] C. E. Shannon, "Communication in the presence of noise," *Proc. IRE*, vol. 37, no. 1, pp. 10–21, Jan. 1949.

[28] *CYGNSS Handbook Cyclone Global Navigation Satellite System: Deriving Surface Wind Speeds in Tropical Cyclones*. Ann Arbor, MI, USA: Univ. Michigan, 2016. [Online]. Available: http://www.publishing.umich.edu/services/

[29] CYGNSS Level 1 science data record version 2.1, PO.DAAC, Pasadena, CA, USA, 2017. [Online]. Available: https://podaac.jpl.nasa.gov/dataset/CYGNSS_L1_V2.1

[30] EUMETSAT OSI-SAF. [Online]. Available: http://www.osi-saf.org/?q=content/wind-products

[31] *ScatSat-1 wind product user manual, SAF/OSI/CDOP2/KNMI/TEC/MA/287, version 1.3*. EUMETSAT OSI-SAF. (2018). [Online]. Available: http://projects.knmi.nl/scatterometer/publications/pdf/osisaf_cdop2_ss3_pum_scatsat1_winds.pdf

[32] F. Fabra, E. Cardellach, W. Li, and A. Rius, "WAVPY: A GNSS-R open source software library for data analysis and simulation," in *Proc. IEEE Int. Geosci. Remote Sens. Symp.*, Jul. 2017, pp. 4125–4128.

[33] E. Cardellach *et al.*, "Consolidating the precision of interferometric GNSS-R ocean altimetry using airborne experimental data," *IEEE Trans. Geosci. Remote Sens.*, vol. 52, no. 8, pp. 4992–5004, Aug. 2014.

Giuseppe Grieco received the M.Sc. degree in marine sciences from the Parthenope University of Naples, Naples, Italy, in 2001, and the Ph.D. degree in environmental engineering from Università della Basilicata, Potenza, Italy, in 2008.

Currently, he has a EUMETSAT fellowship on GNSS reflectometry that is being carried out at Koninklijk Nederlands Meteorologisch Instituut, De Bilt, The Netherlands, in collaboration with the Institute of Marine Sciences, Barcelona, Spain.

Ad Stoffelen (Senior Member, IEEE) received the M.Sc. degree in physics from the Eindhoven University of Technology, Eindhoven, The Netherlands, in 1987, and the Ph.D. degree in meteorology on scatterometry from Utrecht University, Utrecht, The Netherlands, in 1998.

He currently leads a group on active satellite sensing at Koninklijk Nederlands Meteorologisch Instituut, De Bilt, The Netherlands, and is involved in topics ranging from future missions and R&D for retrieval to 24/7 operations, NWP mesoscale wind data assimilation, user training and services. Establishing an international scatterometer virtual constellation is one of his main aims. He is also deeply involved in the ESA ADM-Aeolus Doppler Wind Lidar mission.

Marcos Portabella was born in Spain on October 14, 1970. He received the B.Sc. degree in physics from the University of Barcelona, Barcelona, Spain, in 1994, the M.Sc. degree in remote sensing from the Institute of Space Studies of Catalonia, Barcelona, in 1995, and the Ph.D. degree in physics from the University of Barcelona in 2002.

He is currently with the Institute of Marine Sciences, Barcelona, working on satellite remote sensing. In particular, he is involved in scatterometry and *L*-band radiometry.